

Selected Negative Linear Compressibilities in the Metal–Organic Framework of $[\text{Cu}(4,4'\text{-bpy})_2(\text{H}_2\text{O})_2]\cdot\text{SiF}_6$ Zhongwei Chen,[‡] Bin Xu,[‡] Qian Li,^{*} Yue Meng, Zewei Quan, and Bo ZouCite This: <https://dx.doi.org/10.1021/acs.inorgchem.9b02884>

Read Online

ACCESS |



Metrics & More

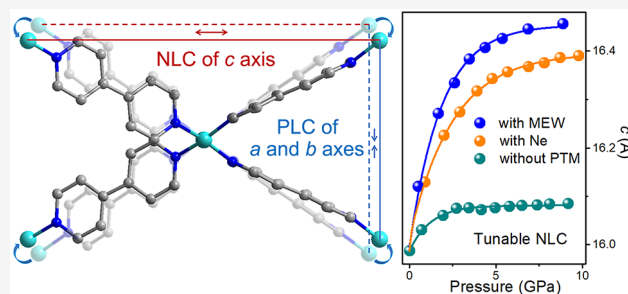


Article Recommendations



Supporting Information

ABSTRACT: Negative linear compressibility (NLC) is a rare high-pressure observation that lattice contraction is accompanied by the structural expansion along a specific direction. Generally, this counterintuitive phenomenon only derives from the intrinsic structural characteristics of materials and cannot be tuned by external perturbations. Searching for an effective method to control NLC effect is still a challenge in both chemical and material science. Here, we successfully discover and select the NLC behaviors in the metal–organic framework (MOF) of $[\text{Cu}(4,4'\text{-bpy})_2(\text{H}_2\text{O})_2]\cdot\text{SiF}_6$ ($\text{Cu}(\text{bpy})\cdot\text{SiF}$) through controlling the pressure conditions therein. The NLC effect of $\text{Cu}(\text{bpy})\cdot\text{SiF}$ originates from the wine-rack mechanism that quasi-square grids transfer to rhombic ones with the structural expansion along the diagonal direction at high pressure. Meanwhile, both of the pressure range and magnitude of the NLC responses are enlarged with optimized pressure conditions. This study not only presents the intriguing selected NLC behaviors of a MOF but also proves the effects of pressure conditions on NLC, which offers promising strategies for further design and applications of NLC materials.



INTRODUCTION

In the common sense of thermodynamic dictates, material structures are inevitably contracted in all directions upon increasing pressure. Whereas, a handful of exceptional materials exhibit counterintuitive structural responses at high pressure that volume reduction is accompanied by the structural expansion along a specific direction.¹ This rare phenomenon is termed as negative linear compressibility (NLC), which has attracted increasing attention in recent years.^{2,3} The intense interest of NLC not only arises from its unique structural mechanisms for fundamental explorations but also from the promising exploitations of NLC materials in devices. Materials with proper NLC properties are coveted for developing high-sensitivity pressure detectors, pressure-driven actuators, artificial muscles, optical telecommunication cables, etc.^{4–7} However, the currently observed NLC behaviors are all dependent on the intrinsic structural features of materials and cannot be tuned by external perturbations. To date, the tunable NLC effect has only been realized by varying the inorganic component of the MFM-133(M) (M = Zr, Hf) without changing the framework topology.⁸ It is still a big challenge to modulate the intrinsic NLC responses of one targeted material through controlling the pressurization process. Searching for an effective method to affect the NLC behaviors of materials without component modifications and getting a deeper insight into the structure–property relationships therein have become the urgently solved problems in further NLC explorations.

Early reported NLC phenomena mainly focus on simple inorganic and organic systems, which are induced by the phase transition, framework tilting, and helices expansion of the structures (Table S1–S3).^{9–14} Recently, NLC studies have been extended to organic–inorganic hybrid systems (Table S4),^{15–18} and a novel family of metal–organic frameworks (MOFs) is emerging as a rising star in this new category of NLC materials. In the aesthetic architectures of MOFs, the rigid linker of organic ligands is flexibly coordinated to the metal hinges, which are greatly conducive to the NLC effects with framework hinging mechanism (Table S5).¹⁹ The framework hinging mechanism involves the densification of one crystal direction and structural expansion in its vertical directions with increasing pressure.²⁰ It is essentially related to the specific framework topologies of materials, such as wine-rack,^{21–24} scissor-like,^{16,19} butterfly wing,²⁵ honeycomb,^{2,9,11,12} and β -quartz.²⁶ In high-pressure MOFs, this mechanism has induced various unique NLC responses, including the considerably high degree of NLC effect with a compressibility of -28 TPa^{-1} below 3 GPa.²¹

With increasing pressure, framework hinging NLC in MOFs is realized through the framework distortion and channels/pores modulation within the structures, which greatly depend

Received: September 27, 2019

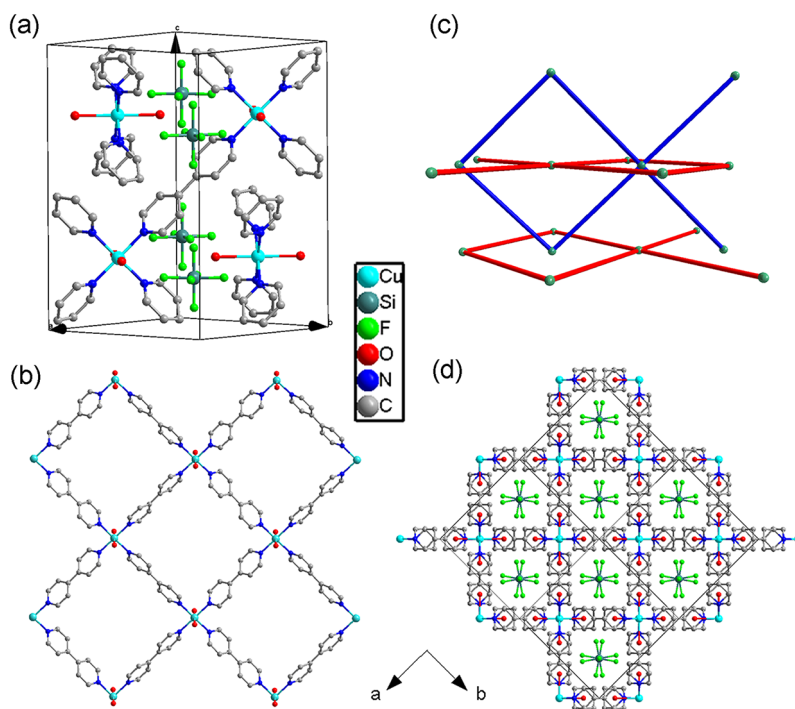


Figure 1. Crystal structure of Cu(bpy)·SiF at ambient conditions. The hydrogen atoms are omitted for clarity. (a) One unit cell of Cu(bpy)·SiF. (b) The 2D metal–organic networks of Cu(4,4'-bpy)₂(H₂O)₂ with quasi-square grids. (c) Topology of interpenetrated frameworks, in which the balls and sticks represent the coordinated Cu centers and 4,4'-bpy ligands, respectively. Different colors represent different sets of 2D networks in (b). (d) Structural view of the whole framework along *c* axis.

on the force balance in three dimensions. Thus, the framework hinging distortion in MOFs is more likely influenced by the external perturbations of the force state modulation.²⁷ It is expected that the unique structural nature of MOFs may offer some new possibilities for the controlled NLC effects through tuning the pressurization methods on the materials, making them promising candidates for the next-generation NLC materials. In high-pressure experiments, the stress state of the sample is easily affected by tuning the pressure transmitting media (PTM) around the sample. With proper PTM, the samples can be compressed under hydrostatic and quasi-hydrostatic pressure conditions. Experimental results under hydrostatic compression mainly exhibit the intrinsic material properties, avoiding the influences of inhomogeneous compression, differential (mostly uniaxial) and shear stresses.^{28,29} Meanwhile, without PTM, the samples are compressed in nonhydrostatic pressure conditions. The nonhydrostatic compression not only includes the contributions from the hydrostatic pressure component but also contains the effects of deviatoric stress component. The poorer pressure conditions may induce some anomalous structural behaviors and mechanical properties, which depart from the hydrostatic compression results.³⁰ Therefore, there is the question of whether the deviatoric stress on the MOFs can affect the NLC behaviors of the systems? Meanwhile, is it possible to select the NLC responses of MOFs through the modulation of pressure conditions?

To realize the selected NLC behaviors at high pressure, in this work, we combine high-pressure Raman, angle dispersive X-ray diffraction (ADXRD) techniques and first-principle calculations together, discovering a new NLC material of MOF, [Cu(4,4'-bpy)₂(H₂O)₂]·SiF₆ (Cu(bpy)·SiF). Note that both the magnitude and pressure range of NLC behaviors in

Cu(bpy)·SiF are successfully modulated by changing the pressure conditions around the sample. With hydrostatic pressure conditions, the NLC behaviors of Cu(bpy)·SiF are observed in a pressure range as broad as ~10 GPa. This is the first observation of selected NLC effects at high pressure with such a broad pressure range. It is expected that this study can not only provide an in-depth understanding of NLC properties but also offer promising strategies for the further design and applications of NLC materials.

EXPERIMENTAL DETAILS

Syntheses of [Cu(4,4'-bpy)₂(H₂O)₂]·SiF₆ (Cu(bpy)·SiF). The Cu(bpy)·SiF sample was prepared according to the procedures reported previously.³¹ Cu(BF₄)₂·xH₂O (1.0 mmol) and (NH₄)₂SiF₆ (1.0 mmol) were dissolved into the host aqueous solution (10 mL), and then the solution was added into another host aqueous solution (10 mL) of 4,4'-bpy (2.0 mmol). During stirring, the obtained purple suspension gradually transferred to sky-blue. After filtering the suspension, we got the sky-blue powder and washed it with acetone for several times. Then, the sample was dried in air, forming the microcrystals. Sample purity was confirmed by the X-ray diffraction pattern.

High-Pressure Sample Loading. The symmetric diamond anvil cell (DAC), equipped with 0.4 mm diamond culets, was applied for high-pressure generation. The powdered sample was loaded into the sample compartment, a 150 μm-diameter aperture at the center of a preindented rhenium gasket, with ruby balls for the pressure calibration.³² High-pressure experiments were performed without pressure transmitting media (PTM) and with neon (Ne) and 16:3:1 methanol–ethanol–water (MEW) as PTM, so as to guarantee the different pressure conditions according to the Pascal principle. All of the experiments were performed at room temperature.

High-Pressure Experiments. High-pressure angle dispersive X-ray diffraction (ADXRD) measurements were performed at Sector 16-IDB of High Pressure Collaborative Access Team (HPCAT),

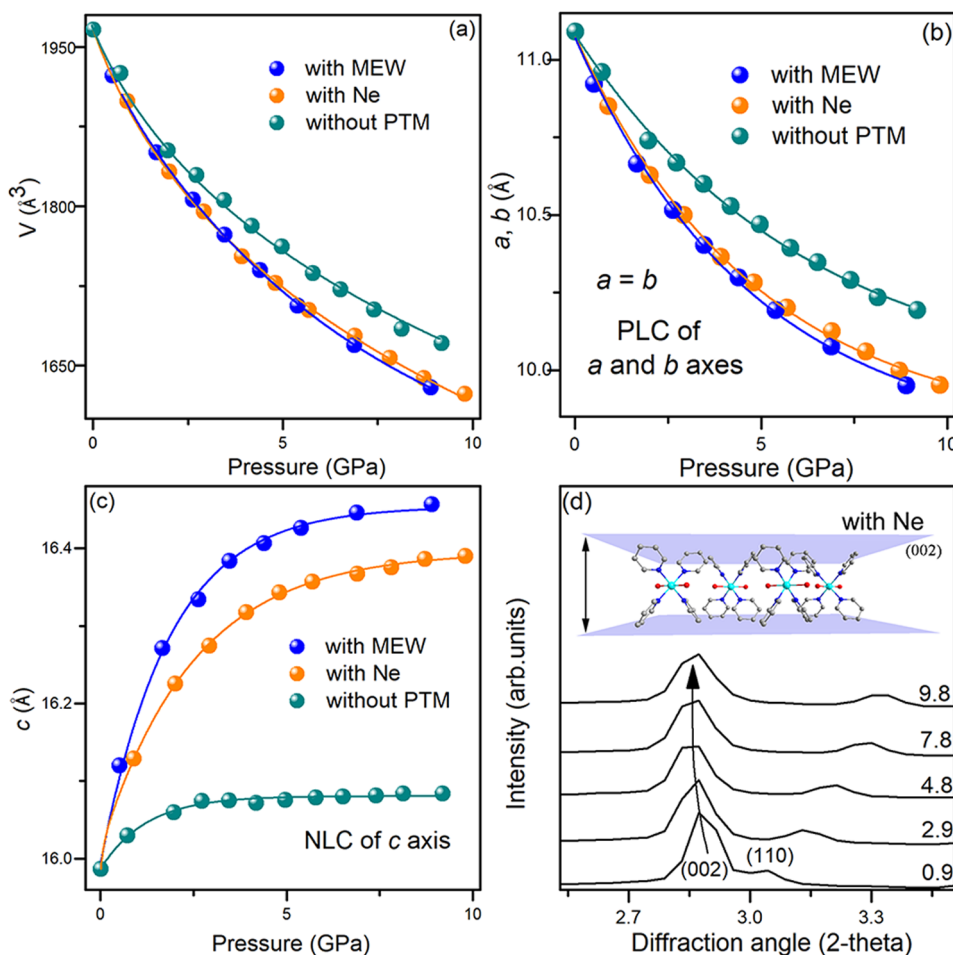


Figure 2. High-pressure evolution of (a) unit cell volume, (b) a and b axes, and (c) c axis below ~ 10 GPa. The fitting curves are only used to clarify the evolution trends of lattice parameters. (d) High-pressure diffraction patterns of (002) and (110) with Ne as PTM. The inset shows the Miller planes of (002).

Advanced Photon Source (APS). The monochromatic wavelength was 0.4066 \AA and beamsize was $\sim 4 \times 5 \mu\text{m}^2$. Before each experiment, CeO_2 was used for the calibration of geometric parameters. The two-dimensional (2D) Bragg diffraction rings were recorded with a Pilatus detector and converted into one-dimensional (1D) patterns using Fit2D software.³³ Further analysis of ADXRD data, which provided high-pressure structural information, was performed using the commercial program of Materials Studio 5.5. The linear compressibilities of the NLC axis were obtained by error-weighted fitting of the lattice parameters with the PASCAL software from <http://pascal.chem.ox.ac.uk/>, using the empirical form $l = l_0 + \lambda(p - p_c)^{\nu}$.³⁴ High-pressure unpolarized Raman experiments were also conducted using the laser with wavelength of 532 nm at HPCAT.

High-Pressure Calculation. Ab initio calculations were carried out based on the ambient structural model reported before.³¹ The water molecules were omitted during the calculation for the simplification. Pseudopotential plane-wave method based on the density functional theory was adopted by applying the CASTEP code combined in the Materials Studio program. Local density approximation exchange–correlation functional and BFGS algorithm were applied for structural optimization. The plane-wave cutoff energy and Monkhorst–Pack grid for the electronic Brillouin zone integration were 330 eV and $2 \times 2 \times 1$, respectively. The self-consistent field (SCF) tolerance was set as $1.0 \times 10^{-6} \text{ eV/atom}$, and the calculation was ended when the stress components and forces on the atoms were $< 0.05 \text{ GPa}$ and 0.03 eV/\AA , respectively.

RESULTS AND DISCUSSION

At ambient conditions, $\text{Cu}(\text{bpy}) \cdot \text{SiF}_6$ exhibits a typical MOF structure with three-dimensional (3D) interpenetrated networks, which belongs to tetragonal space group of $P4/ncc$ symmetry with unit cell parameters of $a = b = 11.08(0) \text{ \AA}$, $c = 16.02(4) \text{ \AA}$.³¹ As shown in Figure 1a, the four nitrogen atoms of 4,4'-bipyridine (4,4'-bpy) ligands and two oxygen atoms of H_2O molecules are coordinated to one Cu atom, leading to the elongated octahedral coordination environment of Cu centers, and the coordinated Cu ions are bridged by the 4,4'-bpy ligands, forming the 2D metal–organic networks with quasi-square grids (Figure 1b). The 3D structure of $\text{Cu}(\text{bpy}) \cdot \text{SiF}_6$ is just constructed by the perpendicular interpenetration of such 2D networks with the microporous channels along c axis (Figure 1c). Besides, free SiF_6^{2-} dianions are located in the channels (Figure 1d), interacting with the coordinated H_2O molecules through hydrogen bonds. The $\text{Cu}(\text{bpy}) \cdot \text{SiF}_6$ exhibits a typical wine-rack motif, which confirms the topological demands for wine-rack NLC mechanism. The flexible coordination hinges of Cu are also a benefit for the framework distortion at high pressure. Furthermore, the interpenetrated frameworks, as well as the SiF_6^{2-} guest anions within the channels, could together contribute to the mechanical stability, allowing structural research in a relatively broad pressure range.³⁵

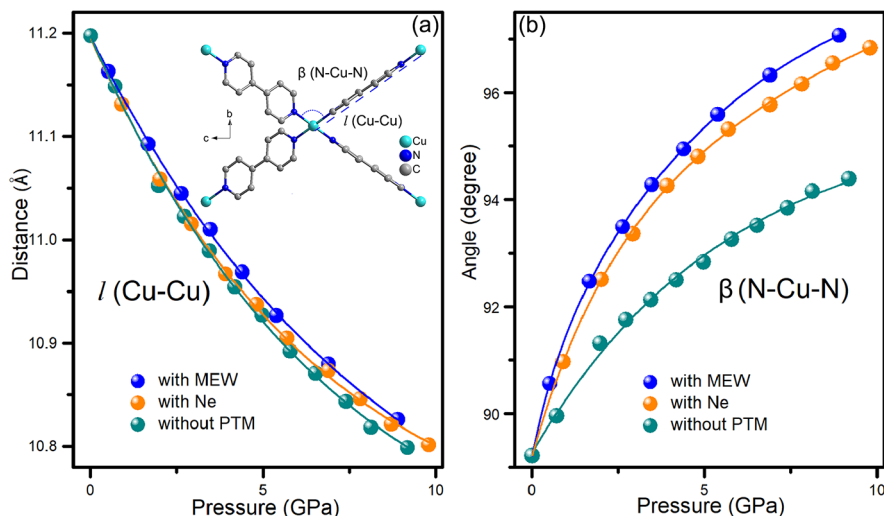


Figure 3. High-pressure evolution of interatomic distance $l(\text{Cu}-\text{Cu})$ and bond angle $\beta(\text{N}-\text{Cu}-\text{N})$ below ~ 10 GPa. The fitting curves are only used to clarify the evolution trends of structure parameters.

High-pressure ADXRD experiments offer straightforward information on structural evolution. The ambient diffraction signal of $\text{Cu}(\text{bpy})\cdot\text{SiF}$ and identification of its diffraction peaks are shown in Figure S1. The Rietveld refinements of ambient ADXRD patterns are shown in Figure S2. The ADXRD experiments of $\text{Cu}(\text{bpy})\cdot\text{SiF}$ are first conducted without any PTM, showing structural responses under nonhydrostatic conditions. During compression, all diffraction peaks shift to higher angles, except the lower-angle shifts of (002) peak below ~ 3.5 GPa (Figure S3). It reflects that with the constriction of the whole $\text{Cu}(\text{bpy})\cdot\text{SiF}$ architecture, the space between (002) Millar planes is abnormally expanded in this pressure range.³⁶ Pressure dependence of lattice parameters also shows that a and b axes and cell volume are all contracted with increasing pressure (Figure 2a,b), but the c axis displays obvious expansion up to ~ 3.5 GPa (Figure 2c), demonstrating the NLC effect along the c -axis direction. With further compression up to ~ 10 GPa, there is no obvious change in the length of c axis, implying the quasi-equilibrium state between the expansion and contraction of the condensed structures along c axis. This phenomenon is not commonly seen in high-pressure materials.¹⁶ Furthermore, after releasing pressure, the ADXRD pattern of $\text{Cu}(\text{bpy})\cdot\text{SiF}$ returns to its original state, suggesting the reversibility of this NLC effect (Figure S4).

In another two runs of ADXRD experiments, neon (Ne) and 16:3:1 MEW mixtures are applied as PTM, respectively (Figures S5 and S6). The corresponding Rietveld refinements of ADXRD patterns and detailed lattice parameters at high pressure are shown in Figures S7–S9 and Tables S6–S8. At 300 K, MEW exhibits a glass transition at 14.4 GPa and Ne crystallizes at only 4.8 GPa. The high-pressure experiments with MEW as PTM adopt the better pressure conditions than that with Ne.²⁸ In these two sets of experiments, a and b axes as well as lattice volume of $\text{Cu}(\text{bpy})\cdot\text{SiF}$ still keep continuous decreasing upon compression, but become more obviously compressed than that without PTM (Figure 2a,b). Importantly, the NLC region with PTM is significantly enlarged. The continuous expansion of the c axis lasts to ~ 10 GPa, which is 6.5 GPa higher than the critical pressure without PTM (Figure 2c,d). Among these three conditions (without PTM, with Ne,

and with MEW), the elongation of c axis with MEW is the largest one corresponding to the best pressure conditions. Meanwhile, it also demonstrates the promotion effect of hydrostatic pressure on the NLC effect in $\text{Cu}(\text{bpy})\cdot\text{SiF}$. In addition, when the highest pressure is increased to ~ 20 GPa, diffraction peaks of $\text{Cu}(\text{bpy})\cdot\text{SiF}$ still keep continuous shifts, showing the highly stable structural nature.³⁶ The c axis with Ne as PTM also exhibits very little contraction (nearly unchanged) above ~ 10 GPa, similar to the $\text{Cu}(\text{bpy})\cdot\text{SiF}$ structural behaviors without PTM between ~ 3.5 and 10 GPa (Figures S10 and S11). It should be noted that the pore-occupying species may influence the structural responses of MOFs. In $\text{Cu}(\text{bpy})\cdot\text{SiF}$, the channels are blocked by the SiF_6^{2-} dianions that the PTM molecules cannot insert into the framework during compression. Meanwhile, at high pressure, the SiF_6^{2-} dianions exhibit little distortion under compression. The Si–F bonds (Si–F1 and Si–F3) are elongated along the c axis, which is the direction of NLC behavior (Figure S12 and Tables S9–S11). The distortion of SiF_6^{2-} dianions may also contribute to the NLC effects of the whole structure. Furthermore, with different pressure conditions, the structural distortions of SiF_6^{2-} dianions are also varied, which is coincident with the selected NLC behaviors.

In order to get more detailed structural information with different pressure conditions, the high-pressure interatomic distances of two adjacent Cu $l(\text{Cu}-\text{Cu})$ and bond angles $\beta(\text{N}-\text{Cu}-\text{N})$ are measured. The high-pressure evolution of $l(\text{Cu}-\text{Cu})$ and $\beta(\text{N}-\text{Cu}-\text{N})$ values present the structure contraction and distortion degree of the quasi-square grids, respectively. As illustrated in Figure 3a, with increasing pressure up to ~ 10 GPa, the two adjacent Cu atoms gradually approach with similar rate in different pressure conditions. The distance between the two N atoms in one bipyridine molecule also exhibits similar contraction behaviors under high pressure (Figure S13). It indicates that pressure conditions have few effects on the linear bond contraction of the $\text{Cu}(\text{bpy})\cdot\text{SiF}$ quasi-square grids. Meanwhile, along with the decrease of bond length, the bond angle of $\beta(\text{N}-\text{Cu}-\text{N})$ is abnormally enlarged as the pressure increasing up to ~ 10 GPa (Figure 3b). Meanwhile, the better pressure conditions promote the expansion of $\beta(\text{N}-\text{Cu}-\text{N})$ during compression, which is

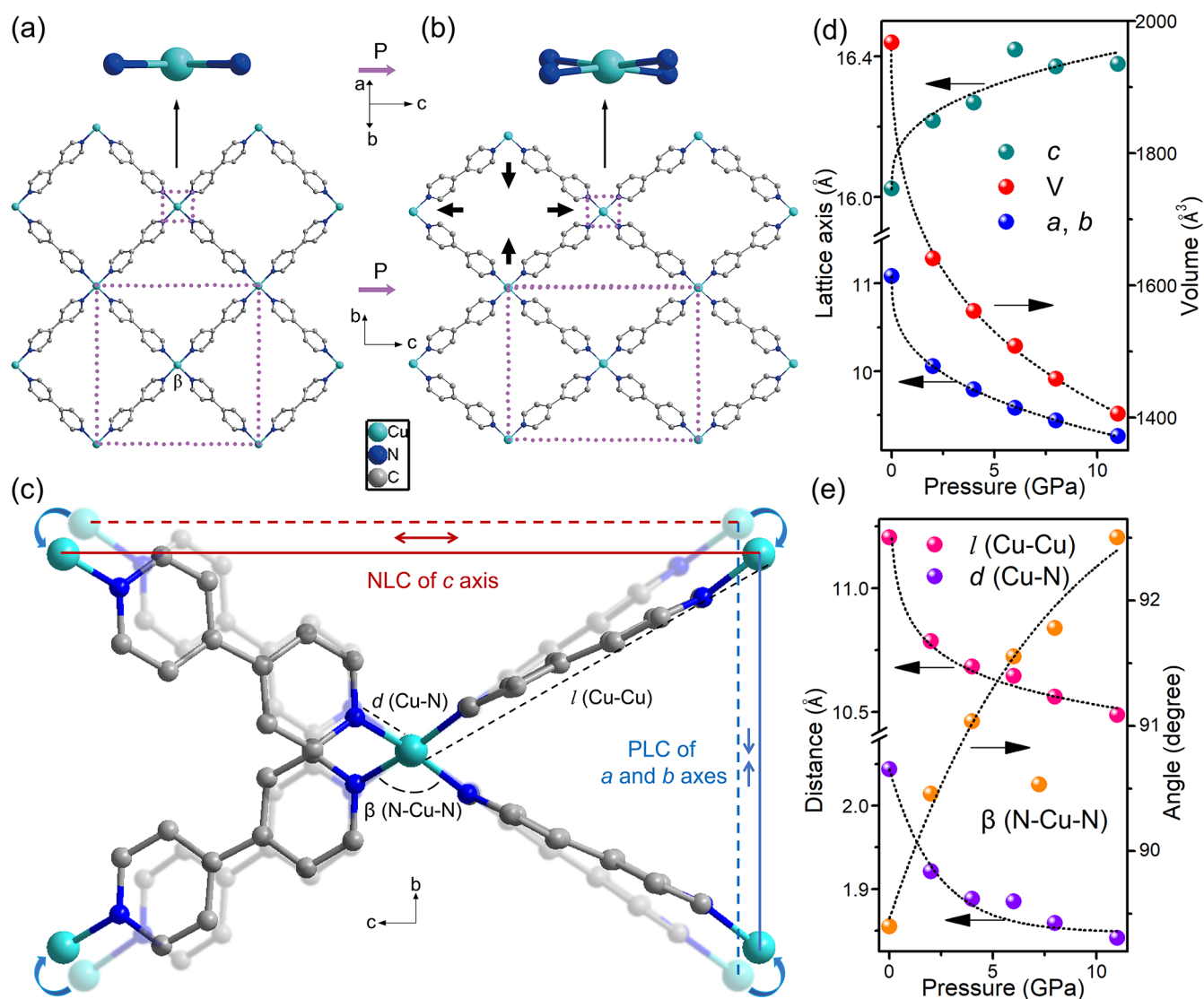


Figure 4. Comparison between 2D networks in the (a) ambient and (b) calculated Cu(bpy)·SiF structure at 11 GPa. (c) Compression mechanism of the framework under pressure. The light-colored molecule indicates the ambient structure, and the dark-colored molecule indicates the calculated structure at 11 GPa. Calculated high-pressure evolution of (d) lattice parameters and (e) Cu–Cu/Cu–N distances and N–Cu–N angles. The lattice axes are fitted by the empirical form $l = l_0 + \lambda(p - p_c)^{\nu}$.

coincident with the most obvious NLC with MEW. Such a phenomenon confirms that the wine-rack mechanism is the main factor for the NLC of Cu(bpy)·SiF. Different pressure conditions induce a varied force balance of the structures, leading to the distorted Cu(bpy)·SiF quasi-square grids with different degrees.

The NLC coefficient, median compressibility of the structures in NLC direction, is widely used to evaluate the NLC value of materials.^{20–26,37} Without PTM, the NLC coefficient of c axis below ~ 3.5 GPa is $K_c = -1.08(9)$ TPa⁻¹ (Table S12), which is comparable with the NLC coefficient of MOF [NH₄][Zn(HCOO)₃] and inorganic element Se.^{24,38} In better pressure conditions, the largest NLC coefficients obtained below ~ 5 GPa are $K_c = -2.83(3)$ TPa⁻¹ (with Ne) and $K_c = -3.56(9)$ TPa⁻¹ (with MEW), respectively (Tables S13 and S14). These parameters are two and three times larger than that without PTM, showing the considerable NLC tuning effects of pressure conditions. In the whole NLC range up to ~ 10 GPa with PTM, the NLC coefficients K_c become smaller

($-1.48(3)$ TPa⁻¹ with Ne and $-2.08(1)$ TPa⁻¹ with MEW, Tables S15 and S16) than that up to ~ 5 GPa, as a result of the more compact structure in higher pressure range.³⁷ Furthermore, P – V data evolution is a powerful clue to explore the high-pressure mechanical properties of Cu(bpy)·SiF structure. Bulk modulus B_0 and its first-order derivative B' are obtained by the third-order Birch–Murnaghan equation of state (EOS) fitting of P – V data (Figure S14). The relatively larger B' ($\gg 4$) represents the rapid stiffening process of the Cu(bpy)·SiF framework and its significant pressure sensitivity during compression.³⁹ Meanwhile, for comparison, when B' is fixed at 4, B_0 gradually decreases from 40.90(4) to 33.45(6) along with the improvement in pressure conditions, which is coincident with the more easily compressed structural property in better pressure conditions. Compared with other MOFs, the relatively low B_0 reflects the high compressibility of Cu(bpy)·SiF.^{22–24} Therefore, it is inferred that the considerable pressure compressibility and sensitivity, as well as the outstanding

stability of the structure, together contribute to the large pressure range of NLC effect in Cu(bpy)·SiF.

In order to obtain the more detailed local structural information, high-pressure Raman experiments with different pressure conditions are conducted on Cu(bpy)·SiF. As seen in Figures S15–S17, with increasing pressure, one ring breathing mode is intensified and exhibits unique redshifts up to ~10 GPa, suggesting the gradual distortion of the molecular rings of 4,4'-bipyridine.^{36,37} Meanwhile, the four $\nu(\text{O-H})$ modes keep blueshifts with their initial relative intensities and shapes during compression, reflecting the high-pressure enhancement and stabilization of hydrogen bonding networks.¹⁰ Note that the Si–F bonds along the c axis are not involved in the hydrogen bondings in Cu(bpy)·SiF. Hence, the continuously enhanced hydrogen bonds could contribute to the elongated SiF_6^{2-} dianions along the c axis, which is coincident with the results of ADXR experiments. In addition, the enhanced hydrogen bonds may also contribute to the considerable structural stability of Cu(bpy)·SiF.³⁶

Based on the ADXR and Raman experiments, first-principle calculations are performed to characterize the structural variations of Cu(bpy)·SiF. At high pressure, there is no obvious conformation change in the guest SiF_6^{2-} dianions, which is in accordance with the continuous evolution of $\nu(\text{O-H})$ Raman modes. Meanwhile, just as the observed NLC phenomena in ADXR experiments, the 2D quasi-square grids (corner angles of ~91° and ~89°) evolve into rhombus-like ones (corner angles of ~103° and ~77°) (Figure 4a–c), accompanied by the expansion of the diagonals along c axis (Figure 4d) and the gradually enlarged β angles of N–Cu–N (Figure 4e). Meanwhile, with increasing pressure, the 4,4'-bpy ligands are distorted slightly, leading to the little puckered molecular configuration (Figure 4a,b). This is coincident with the results deduced from the Raman experiments. Furthermore, the decreased distance between adjacent Cu ions, $l(\text{Cu-Cu})$, represents the linear shrinkage of 4,4'-bpy ligands. At high pressure, although the two pyridine rings are distorted and rotated about the central C–C bond by external force, the 4,4'-bpy ligands still keep the original orientation with linear contraction, exhibiting the rigid contraction nature. For the inorganic hinges, the equatorial planes of the coordinated four nitrogen atoms to Cu ions are distorted slightly, and four Cu–N bond lengths, $d(\text{Cu-N})$, keep continuous shortening all the way up to 11 GPa.

High-pressure structural variations of Cu(bpy)·SiF are coincident with the wine-rack mechanism of NLC effect. In ambient Cu(bpy)·SiF, the squareness deviation of the 2D interpenetrated grids increases the degree of freedom, correspondingly.⁴⁰ Below the critical pressure, with positive compression of the whole structure, the adjustments of N–Cu–N angles in organic hinges induce the distortion of 2D Cu(4,4'-bpy)₂(H₂O)₂ networks from quasi-square to rhombus grids, which is responsible for the NLC effect of c axis. With further compression, the β angles of N–Cu–N are too small that the c axis cannot be expanded anymore. The positive and negative contraction of the c -axis structure competes against each other, leading to the nearly unchanged (little decrease) c axis above the NLC critical pressure. In this pressure range (below ~20 GPa), the contraction and distortion of ligands play leading roles in the shrinkage of lattice axes and cell volume. Meanwhile, framework distortion in Cu(bpy)·SiF depends on the 3D force balance within the structure. In better pressure conditions, the isotropic compression shows the

intrinsic NLC properties of Cu(bpy)·SiF. With PTM, the ~10 GPa pressure range of NLC behavior is rarely seen in NLC materials. Meanwhile, without PTM, the additional deviatoric stress component significantly restrains the structural adjusting process that both the NLC value and range are significantly decreased at high pressure. That is, poorer pressure conditions are able to restrain the NLC process of Cu(bpy)·SiF, just like the inhibiting effects of the phase transitions in some systems.^{41,42} Furthermore, the Cu(bpy)·SiF structure is not a simple wine-rack framework that both of the two perpendicularly interpenetrated 2D network sets exhibit the same responses to high pressure, together contributing to the whole structural stability. The NLC of Cu(bpy)·SiF in such a large pressure range may just result from the flexible, but robust nature of the whole framework.

CONCLUSION

To sum up, we successfully, for the first time, realize the selected NLC effect in the MOF material of Cu(bpy)·SiF at high pressure. The NLC phenomenon in Cu(bpy)·SiF is ascribed to the wine-rack mechanism that the quasi-square grids of the 2D networks are distorted by external force, with the expansion of the diagonals along c axis. Note that both the NLC value and range are significantly increased by optimizing the pressure conditions with different PTM. This study not only offers a promising NLC material of Cu(bpy)·SiF, which exhibits an abnormally large NLC pressure range (~10 GPa) at high pressure, but also proves the great influence of pressure conditions on NLC phenomenon. It indicates that the influences of deviatoric stress have to be taken into consideration for the further design, synthesis, and applications of NLC materials. Furthermore, we infer that the unique flexible and rigid nature of the MOF structure may offer some more abnormal compression behaviors in the following explorations.

ASSOCIATED CONTENT

Supporting Information

The Supporting Information is available free of charge at <https://pubs.acs.org/doi/10.1021/acs.inorgchem.9b02884>.

Additional ADXR, Raman spectra and calculation results, and detailed data analysis (PDF)

AUTHOR INFORMATION

Corresponding Author

Qian Li – Department of Chemistry, Academy for Advanced Interdisciplinary Studies, Southern University of Science and Technology (SUSTech), Shenzhen 518055, P.R. China; orcid.org/0000-0002-4847-4892; Email: liq6@sustech.edu.cn

Other Authors

Zhongwei Chen – Department of Chemistry, Academy for Advanced Interdisciplinary Studies, Southern University of Science and Technology (SUSTech), Shenzhen 518055, P.R. China; orcid.org/0000-0002-9558-6969

Bin Xu – Department of Chemistry, Academy for Advanced Interdisciplinary Studies, Southern University of Science and Technology (SUSTech), Shenzhen 518055, P.R. China

Yue Meng – HPCAT, X-ray Science Division, Argonne National Laboratory, Argonne, Illinois 60439, United States

Zwei Quan – Department of Chemistry, Academy for Advanced Interdisciplinary Studies, Southern University of Science and Technology (SUSTech), Shenzhen 518055, P.R. China; orcid.org/0000-0003-1998-5527

Bo Zou – State Key Laboratory of Superhard Materials, College of Physics, Jilin University, Changchun 130012, P.R. China; orcid.org/0000-0002-3215-1255

Complete contact information is available at:

<https://pubs.acs.org/10.1021/acs.inorgchem.9b02884>

Author Contributions

[‡]These authors contributed equally to this work.

Notes

The authors declare no competing financial interest.

ACKNOWLEDGMENTS

This work is supported by the National Natural Science Foundation of China (NSFC) (nos. 11604141, 21673100, 21725304) and Chang Jiang Scholars Program (no. T2016051). ADXRD measurements were performed at the High Pressure Collaborative Access Team (HPCAT 16-IDB), APS, ANL. HPCAT operations are supported by DOE-NNSA's Office of Experimental Sciences. The Advanced Photon Source is a U.S. Department of Energy (DOE) Office of Science User Facility operated for the DOE Office of Science by Argonne National Laboratory under contract no. DE-AC02-06CH11357

REFERENCES

- (1) Baughman, R. H.; Stafström, S.; Cui, C.; Dantas, S. O. Materials with negative compressibilities in one or more dimensions. *Science* **1998**, *279*, 1522–1524.
- (2) Grima, J. N.; Attard, D.; Caruana-Gauci, R.; Gatt, R. Negative linear compressibility of hexagonal honeycombs and related systems. *Scr. Mater.* **2011**, *65*, 565–568.
- (3) Ortiz, A. U.; Boutin, A.; Fuchs, A. H.; Coudert, F.-X. Anisotropic elastic properties of flexible metal-organic frameworks: how soft are soft porous crystals? *Phys. Rev. Lett.* **2012**, *109*, 195502.
- (4) Spinks, G. M.; Wallace, G. G.; Fifield, L. S.; Dalton, L. R.; Mazzoldi, A.; De Rossi, D.; Khayrullin, I. I.; Baughman, R. H. Pneumatic carbon nanotube actuators. *Adv. Mater.* **2002**, *14*, 1728–1732.
- (5) Aliev, A. E.; Oh, J.; Kozlov, M. E.; Kuznetsov, A. A.; Fang, S.; Fonseca, A. F.; Ovalle, R.; Lima, M. D.; Haque, M. H.; Gartstein, Y. N.; Zhang, M.; Zakhidov, A. A.; Baughman, R. H. Giant-stroke, superelastic carbon nanotube aerogel muscles. *Science* **2009**, *323*, 1575–1578.
- (6) Cairns, A. B.; Goodwin, A. L. Negative linear compressibility. *Phys. Chem. Chem. Phys.* **2015**, *17*, 20449–20465.
- (7) Ghaedizadeh, A.; Shen, J.; Ren, X.; Xie, Y. M. Designing composites with negative linear compressibility. *Mater. Des.* **2017**, *131*, 343–357.
- (8) Yan, Y.; O'Connor, A. E.; Kanthasamy, G.; Atkinson, G.; Allan, D. R.; Blake, A. J.; Schröder, M. Unusual and tunable negative linear compressibility in the metal-organic framework MFM-133 (M)(M=Zr, Hf). *J. Am. Chem. Soc.* **2018**, *140*, 3952–3958.
- (9) Fortes, A. D.; Suard, E.; Knight, K. S. Negative linear compressibility and massive anisotropic thermal expansion in methanol monohydrate. *Science* **2011**, *331*, 742–746.
- (10) Qiao, Y.; Wang, K.; Yuan, H.; Yang, K.; Zou, B. Negative linear compressibility in organic mineral ammonium oxalate monohydrate with hydrogen bonding wine-rack motifs. *J. Phys. Chem. Lett.* **2015**, *6*, 2755–2760.
- (11) Cairns, A. B.; Catafesta, J.; Levelut, C.; Rouquette, J.; Van Der Lee, A.; Peters, L.; Thompson, A. L.; Dmitriev, V.; Haines, J.; Goodwin, A. L. Giant negative linear compressibility in zinc dicyanoaurate. *Nat. Mater.* **2013**, *12*, 212–216.
- (12) Goodwin, A. L.; Keen, D. A.; Tucker, M. G. Large negative linear compressibility of Ag₃[Co(CN)₆]. *Proc. Natl. Acad. Sci. U. S. A.* **2008**, *105*, 18708–18713.
- (13) Cairns, A. B.; Thompson, A. L.; Tucker, M. G.; Haines, J.; Goodwin, A. L. Rational design of materials with extreme negative compressibility: Selective soft-mode frustration in KMn[Ag(CN)₂]₃. *J. Am. Chem. Soc.* **2012**, *134*, 4454–4456.
- (14) Duyker, S. G.; Peterson, V. K.; Kearley, G. J.; Studer, A. J.; Kepert, C. J. Extreme compressibility in LnFe(CN)₆ coordination framework materials via molecular gears and torsion springs. *Nat. Chem.* **2016**, *8*, 270–275.
- (15) Woodall, C. H.; Beavers, C. M.; Christensen, J.; Hatcher, L. E.; Intissar, M.; Parlett, A.; Teat, S. J.; Reber, C.; Raithby, P. R. Hingeless negative linear compression in the mechanochromic gold complex [(C₆F₅Au)₂(μ-1,4-diisocyanobenzene)]. *Angew. Chem.* **2013**, *125*, 9873–9876.
- (16) Shepherd, H. J.; Palamarciuc, T.; Rosa, P.; Guionneau, P.; Molnár, G.; Létard, J.-F.; Bousseksou, A. Antagonism between extreme negative linear compression and spin crossover in [Fe(dpp)₂(NCS)₂]₂·py. *Angew. Chem., Int. Ed.* **2012**, *51*, 3910–3914.
- (17) Colmenero, F.; Cobos, J.; Timón, V. Negative linear compressibility in uranyl squarate monohydrate. *J. Phys.: Condens. Matter* **2019**, *31* (17), 175701.
- (18) Yeung, H. H.; Kilmurray, R.; Hobday, C. L.; McKellar, S. C.; Cheetham, A. K.; Allan, D. R.; Moggach, S. A. Hidden negative linear compressibility in lithium l-tartrate. *Phys. Chem. Chem. Phys.* **2017**, *19* (5), 3544–3549.
- (19) James, S. L. Metal-organic frameworks. *Chem. Soc. Rev.* **2003**, *32*, 276–288.
- (20) Ogborn, J. M.; Collings, I. E.; Moggach, S. A.; Thompson, A. L.; Goodwin, A. L. Supramolecular mechanics in a metal-organic framework. *Chem. Sci.* **2012**, *3*, 3011–3017.
- (21) Serra-Crespo, P.; Dikhtiarenko, A.; Stavitski, E.; Juan-Alcañiz, J.; Kapteijn, F.; Coudert, F.-X.; Gascon, J. Experimental evidence of negative linear compressibility in the MIL-53 metal-organic framework family. *CrystEngComm* **2015**, *17*, 276–280.
- (22) Cai, W.; Katrusiak, A. Giant negative linear compression positively coupled to massive thermal expansion in a metal-organic framework. *Nat. Commun.* **2014**, *5*, 4337.
- (23) Ortiz, A. U.; Boutin, A.; Gagnon, K. J.; Clearfield, A.; Coudert, F. X. Remarkable pressure responses of metal-organic frameworks: proton transfer and linker coiling in zinc alkyl gates. *J. Am. Chem. Soc.* **2014**, *136*, 11540–11545.
- (24) Li, W.; Probert, M. R.; Kosa, M.; Bennett, T. D.; Thirumurugan, A.; Burwood, R. P.; Parinello, M.; Howard, J. A.; Cheetham, A. K. Negative linear compressibility of a metal-organic framework. *J. Am. Chem. Soc.* **2012**, *134*, 11940–11943.
- (25) Zielinski, W.; Katrusiak, A. Colossal Monotonic Response to hydrostatic pressure in molecular crystal induced by a chemical modification. *Cryst. Growth Des.* **2014**, *14*, 4247–4253.
- (26) Zeng, Q.; Wang, K.; Zou, B. Large Negative Linear Compressibility in InH(BDC)₂ from Framework Hinging. *J. Am. Chem. Soc.* **2017**, *139*, 15648–15651.
- (27) Ortiz, A. U.; Boutin, A.; Fuchs, A. H.; Coudert, F.-X. Metal-organic frameworks with wine-rack motif: What determines their flexibility and elastic properties? *J. Chem. Phys.* **2013**, *138*, 174703.
- (28) Klotz, S.; Chervin, J.-C.; Munsch, P.; Le Marchand, G. Hydrostatic limits of 11 pressure transmitting media. *J. Phys.: Appl. Phys.* **2009**, *42*, 075413.
- (29) Wang, Y.; Zhou, Z.; Wen, T.; Zhou, Y.; Li, N.; Han, F.; Xiao, Y.; Chow, P.; Sun, J.; Pravica, M.; Cornelius, A. L.; Yang, W.; Zhao, Y. Pressure-driven cooperative spin-crossover, large-volume collapse, and semiconductor-to-metal transition in manganese(II) honeycomb lattices. *J. Am. Chem. Soc.* **2016**, *138*, 15751–15757.
- (30) Li, Q.; Li, S.; Wang, K.; Liu, J.; Liu, B.; Yang, K.; Zou, B. Pure hexagonal phase of EuF₃ modulated by high pressure. *J. Phys. Chem. C* **2014**, *118*, 7562–7568.

(31) Noro, S.-i.; Kitaura, R.; Kondo, M.; Kitagawa, S.; Ishii, T.; Matsuzaka, H.; Yamashita, M. Framework engineering by anions and porous functionalities of Cu(II)/4,4'-bpy coordination polymers. *J. Am. Chem. Soc.* **2002**, *124*, 2568–2583.

(32) Mao, H. K.; Xu, J.; Bell, P. M. Calibration of the ruby pressure gauge to 800 kbar under quasi-hydrostatic conditions. *J. Geophys. Res.* **1986**, *91*, 4673–4676.

(33) Hammersley, A. P.; Svensson, S. O.; Hanfland, M.; Fitch, A. N.; Hausermann, D. Two-dimensional detector software: From real detector to idealised image or two-theta scan. *High Pressure Res.* **1996**, *14*, 235–248.

(34) Cliffe, M. J.; Goodwin, A. L. PASCAL: a principal axis strain calculator for thermal expansion and compressibility determination. *J. Appl. Crystallogr.* **2012**, *45*, 1321–1329.

(35) Chapman, K. W.; Halder, G. J.; Chupas, P. J. Pressure-induced amorphization and porosity modification in a metal-organic framework. *J. Am. Chem. Soc.* **2009**, *131*, 17546–17547.

(36) Li, Q.; Li, S.; Wang, K.; Liu, J.; Yang, K.; Liu, B.; Zou, G.; Zou, B. High-pressure studies of abnormal guest-dependent expansion in $\{[\text{Cu}(\text{CO}_3)_2](\text{CH}_6\text{N}_3)_2\}_n$. *J. Phys. Chem. C* **2014**, *118*, 5848–5853.

(37) Zeng, Q.; Wang, K.; Qiao, Y.; Li, X.; Zou, B. Negative linear compressibility due to layer sliding in a layered metal-organic framework. *J. Phys. Chem. Lett.* **2017**, *8*, 1436–1441.

(38) Keller, R.; Holzapfel, W. B.; Schulz, H. Effect of pressure on the atom positions in Se and Te. *Phys. Rev. B* **1977**, *16*, 4404–4412.

(39) Zhao, Y.; Von Dreele, R. B.; Weidner, D. J.; Schiferl, D. P-V-T data of hexagonal boron nitride h BN and determination of pressure and temperature using thermoelastic equations of state of multiple phases. *High Pressure Res.* **1997**, *15*, 369–386.

(40) Barnes, D. L.; Miller, W.; Evans, K. E.; Marmier, A. Modelling negative linear compressibility in tetragonal beam structures. *Mech. Mater.* **2012**, *46*, 123–128.

(41) Shen, L. H.; Li, X. F.; Ma, Y. M.; Yang, K. F.; Lei, W. W.; Cui, Q. L.; Zou, G. T. Pressure-induced structural transition in AlN nanowires. *Appl. Phys. Lett.* **2006**, *89*, 141903.

(42) Colonna, N.; Profeta, G.; Continenza, A. Effects of non-hydrostatic pressure on the structural and magnetic properties of BaFe_2As_2 . *Phys. Rev. B: Condens. Matter Mater. Phys.* **2011**, *83*, 224526.